Materials Today Bio 33 (2025) 102068

Contents lists available at ScienceDirect

Materials Today Bio

journal homepage: www.journals.elsevier.com/materials-today-bio

ROS-scavenging hydrogen nanotherapy simultaneously targets inflammation and pain in rheumatoid arthritis

Qiong Wu [a,1], Jian Zhang [b,1], Yu Nan [c], Shixin Zhang [a], Yuyang He [a], Kexin Ye [a], Xiaowen Ruan [d], Sai Kishore Ravi [d,*], Hushan Wang [b,**], Fangfang Chen [a,***]

[a] Key Laboratory of Pathobiology, Ministry of Education, Nanomedicine and Translational Research Center, China-Japan Union Hospital of Jilin University, Changchun, 130033, Jilin, China
[b] Department of Anesthesiology, First Hospital of Jilin University, Changchun, 130021, Jilin, China
[c] Department of Obstetrics and Gynecology, The Second Hospital of Jilin University, Changchun, 130021, Jilin, China
[d] School of Energy and Environment, City University of Hong Kong, 999077, Hong Kong, China

ARTICLE INFO

Keywords:
Hydrogen therapy
Analgesia
Central sensitization
Rheumatoid arthritis
Comprehensive treatment

ABSTRACT

Relieving pain while treating rheumatoid arthritis (RA) is a pressing clinical need to improve satisfaction of patients, which has not received the due attention and solution. Herein, we propose a strategy to kill two birds with one stone, for which we emphasize synergetic therapeutic outcome of analgesia and inhibiting RA progression through introducing hydrogen nanogenerator to scavenge reactive oxygen species (ROS) at lesion locations. This system exhibited efficient ROS scavenging and reducing apoptosis of C17.2 cells. In a complete Freund's Adjuvant-induced RA mouse model, this controlled hydrogen release behavior significantly downregulated pro-inflammatory mediators, protecting chondrocytes from apoptosis and preventing cartilage degradation. Furthermore, hydrogen therapy could effectively restrain the release of inflammatory factors and central sensitization by alleviating mitochondrial dysfunction in peripheral neurons and inhibit NF-κB pathway. Targeting ROS, this approach represents a significant advancement in RA management, offering superior efficacy against nociplastic pain compared to conventional analgesic therapies, providing a novel treatment mode of synergistic anti-inflammatory therapy and pain management.

1. Introduction

Rheumatoid arthritis (RA) is a systemic autoimmune disease characterized by chronic joint inflammation, pain and progressive cartilage degradation [1,2]. Despite advances in RA treatment, clinical studies indicate that 59–79 % of patients continue to experience persistent pain even when inflammatory response is controlled [3]. Chronic inflammation initiates peripheral sensitization, which subsequently induces central sensitization within the central nervous system (CNS) over time [4]. This central sensitization amplifies nociceptive processing in the CNS, rendering patients hypersensitive to nociceptive stimuli that is a pathognomonic feature of nociplastic pain in RA [5]. Importantly, central sensitization responds poorly to conventional analgesics, limiting the effectiveness of standard pain management approaches [6]. Clinical management of RA primarily utilizes non-steroidal anti-inflammatory drugs (NSAIDs, targeting COX enzymes), disease-modifying antirheumatic drugs (DMARDs such as methotrexate and biologics) and glucocorticoids to suppress inflammation and pain, with adjunctive analgesics including acetaminophen or opioids when required. However, these conventional agents usually suffer significant clinical limitations. Chronic NSAID administration associates with gastrointestinal and cardiovascular complications. DMARDs and biologics carry risks of hepatorenal toxicity, myelosuppression and heightened infection susceptibility. Glucocorticoid promotes osteoporosis and metabolic disturbances, while opioid analgesics entail potential addiction and central nervous system adverse effects. Therefore, a dual-targeting therapeutic approach addressing both inflammation and central sensitization is essential to improve treatment outcomes and ultimately enhance patient

* Corresponding author.
** Corresponding author.
*** Corresponding author.
E-mail addresses: skravi@cityu.edu.hk (S.K. Ravi), hswang@jlu.edu.cn (H. Wang), cff@jlu.edu.cn (F. Chen).
[1] The authors contributed equally to this work.

https://doi.org/10.1016/j.mtbio.2025.102068
Received 5 May 2025; Received in revised form 23 June 2025; Accepted 7 July 2025
Available online 10 July 2025

quality of life.

Oxidative stress and inflammation are key contributors to the pathogenesis of RA [7,8]. During disease progression, immune cells within joint tissues such as macrophages become hyperactivated, leading to sustained inflammation [9,10]. Mitochondrial dysfunction and excessive activation of inflammation-related enzymes, such as NADPH oxidase, drive excessive production of reactive oxygen species (ROS) [11]. The accumulation of ROS disrupts chondrocyte homeostasis, induces chondrocyte apoptosis, and contributes to endothelial dysfunction, further exacerbating inflammatory responses and tissue damage [12,13]. Beyond joint pathology, noxious stimuli originating from inflamed joints are transmitted to the spinal cord via peripheral nerves [14]. Additionally, ROS generated in the periphery can reach the dorsal root ganglia (DRG) via the bloodstream or directly act on spinal neurons, altering their excitability and contributing to pain hypersensitivity [15,16]. Within the spinal dorsal horn, an essential relay center for pain processing, ROS augments neuronal excitability by lowering the excitation threshold and enhancing responses to noxious stimuli [17,18]. Moreover, ROS regulates synaptic plasticity in the dorsal horn, reinforcing pain transmission circuits [19]. Under prolonged noxious stimulation, ROS induces excessive presynaptic release of excitatory neurotransmitters like glutamate, while concurrently elevating postsynaptic receptor density or sensitivity, consequently augmenting synaptic efficacy [20]. This persistent modulation of synaptic plasticity amplifies pain signaling within the CNS, leading to the establishment and reinforcement of central sensitization [21]. Given the mechanistic link between ROS, inflammation, and pain sensitization, targeting ROS at lesion sites presents a promising dual-strategy approach for controlling RA progression and alleviating pain. This comprehensive therapeutic paradigm could reduce dependence on conventional painkillers, minimize side effects, and improve patient outcomes.

As an emerging antioxidant gas, hydrogen (H_2) selectively scavenges highly reactive free radicals, such as hydroxyl radicals (•OH) and peroxynitrite ($ONOO^-$), without disrupting normal physiological processes [22]. Recently, several hydrogen-producing nanoplatforms including calcium disilicide nanosheets, Mg-HA motors, and hydrogen-silicon nanosheets [23–25] have been reported to scavenge ROS and suppress inflammatory responses. However, the reported hydrogen nanogenerators commonly suffer from low hydrogen storage capacity and uncontrollable hydrogen release behaviors. Moreover, the therapeutic potential of hydrogen therapy in alleviating RA-related pain and its underlying analgesic mechanism remains substantially underexplored.

Herein, we proposed polydopamine (PDA) nanospheres as an advanced hydrogen carrier that exhibit a strong photothermal effect, well biocompatibility and the capacity to form impermeable barriers encapsulating and isolating environment-sensitive hydrogen storage materials. Hydrogen precursor aminoborane (AB) with high hydrogen storage capacity was further modified on the outer shell layer of PDA to form in situ H_2 nanogenerator PDAB that enables pH- and near-infrared (NIR)-responsive hydrogen generation. PDAB exhibited stable hydrogen supply in response to the mildly acidic RA microenvironment (pH 4.7–6.8) with additional enhancement upon NIR irradiation, ensuring effective scavenging of localized ROS for controlling RA progression and providing synergistic analgesia (see Scheme 1). In the complete Freund's adjuvant-induced arthritis (AIA) mouse model, PDAB + NIR treatment strategy significantly reduced chondrocyte apoptosis and inhibited pathological vascular overgrowth, thereby delaying RA progression. Furthermore, pain behavior assessments and spinal cord immunofluorescence analysis coupled with western blot assay demonstrated that hydrogen therapy alleviated RA pain by reducing central sensitization via ROS/NF-κB pathway. Consequently, this pH/NIR-responsive hydrogen-delivery system based on PDAB nanocomposites demonstrates exceptional safety by circumventing organ toxicity and dependency risks inherent to conventional pharmacotherapy, thus offering a safer paradigm for sustainable disease management.

2. Materials and methods

2.1. Preparation of PDAB

PDAB nanoparticles were synthesized via a one-pot method. Ammonia (0.15 mg) was introduced to a mixture of ethanol (10 mL) and DI water (22.5 mL), and agitated for 30 min. Dopamine hydrochloride (0.105 g) was then added under continuous stirring for 12 h. After

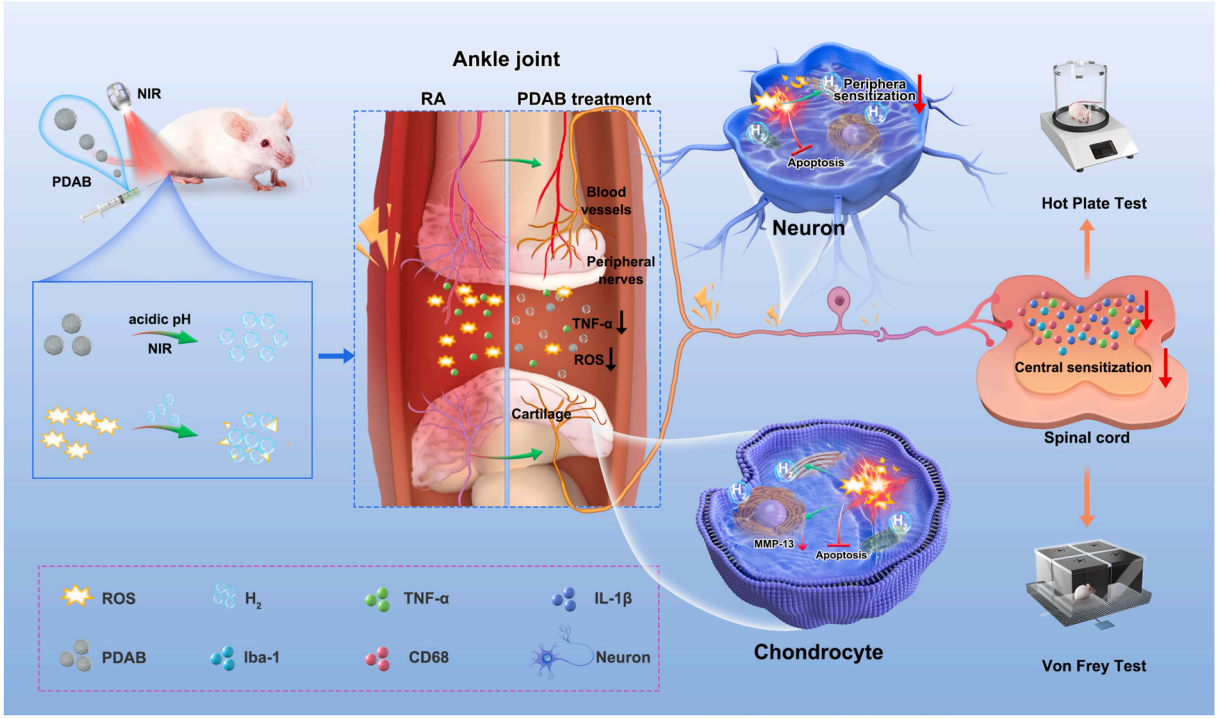

Scheme 1. Schematic illustration of PDAB nanoparticles with NIR-triggered on-demand H_2 release for RA treatment and analgesia in vivo.

introducing AB (0.24 g), the reaction proceeded for 2 h. The reaction mixture was washed once with ethanol and twice with DI water to eliminate unreacted species and byproducts. Finally, the PDAB product was separated by centrifugation and washed with ethanol and deionized water for subsequent applications. PDA was prepared by repeating the above steps without adding AB.

2.2. Hydrogen production assessment

The hydrogen generation levels of PDAB solution was evaluated under different pH values and NIR irradiation via a hydrogen concentration tester. A 50 μL aliquot of 200 μg/mL PDAB solution (pH 5.0) was irradiated with NIR light (1 W/cm^2), then applied to a glass slide and covered with a coverslip. The evolution of H_2 bubble formation and growth dynamics was characterized using inverted microscopy. To quantitatively assess the hydrogen generation kinetics of PDAB under simulated physiological conditions, a methylene blue (MB) reduction assay was implemented. Synovial fluid aspirates were obtained via 0.3 mm diameter capillary puncture of the ankle joint cavity. PDAB solution was introduced into the freshly harvested synovial fluid, followed by NIR irradiation (1 W/cm^2, 5 min). Afterwards, MB solution was introduced, and time-resolved absorbance measurements at 662 nm were performed using a microplate reader at predetermined intervals. Hydrogen production yield and generation rates were derived from the experimentally quantified absorbance decay profiles. Control experiments comprising PBS and PDAB solution treatments were conducted under identical procedural conditions.

2.3. In vitro biosafety

The cytotoxicity of PDAB NPs toward L929 and C17.2 cells was assessed via CCK-8 assay. Briefly, L929 cells (1×10^4 cells/well) were treated with PDAB-containing medium at various concentrations for 24/48 h. For NIR irradiation groups, cells were incubated with PDAB for 4 h, exposed to 808 nm laser (1 W/cm^2, 5 min), then cultured for 20 h. After adding CCK-8 solution (100 μL/well) and 2 h incubation, absorbance at 450 nm was measured. Cell viability was calculated as (ODtreatment − ODblank)/(ODcontrol − ODblank) × 100 %. C17.2 cells were similarly processed using identical procedures.

Live/dead cell staining of L929 cells (5×10^4 cells/well) seeded in 12-well plates overnight was performed using calcein-AM/PI (15 min incubation) and analyzed by fluorescence microscopy.

2.4. In vitro PDAB cellular uptakes

L929 cells in the logarithmic growth phase were seeded in 12-well plates (5×10^4 cells/well), incubated with rhodamine B-modified PDAB (PDAB-RB, 100 μg/mL) for 1, 3, or 5 h, and stained with DAPI for nucleus labeling. Fluorescence imaging was performed using an inverted microscope to analyze RB (red fluorescence) distribution relative to DAPI-stained nuclei (blue fluorescence) within the same field.

2.5. Intracellular hydrogen release measurement and investigation of PDAB bio-reducibility

C17.2 cells (1×10^4 cells/well) were plated in 96-well plates overnight, then stained with MB. After PBS washing, cells were treated with PBS, PDA, or PDAB nanoparticles (100 μg/mL) for 4 h. After PBS washing steps, complete medium supplemented with dissolved hydrogen detection reagent was added, followed by a 10-min incubation period. NIR groups received irradiation (1 W/cm^2, 5 min) using an 808 nm laser. Cellular morphology was documented by inverted microscopy, while quantitative analysis was performed by measuring absorbance at 664 nm using a microplate reader.

2.6. Intracellular ROS clearance and cell viability analysis

L929 cells were seeded in 24-well plates and cultured overnight. Cellular oxidative stress was induced via 20-min H_2O_2 treatment (10 μM), followed by experimental interventions. Intracellular ROS levels were evaluated by analyzing the fluorescence intensity of DCFH-DA. The cells were observed and photographed under a fluorescence microscope, and flow cytometry was used for fluorescence intensity quantification of each group.

C17.2 cells were seeded in 96-well plates at a density of 1×10^4 cells/well and cultured for 24 h. Then, the cells were co-incubated with different treatments for 20 min. The NIR-treated group was irradiated with NIR at a power of 1W/cm^2 for 5 min. Cell viability was determined by the CCK-8 assay, and apoptosis of C17.2 cells was analyzed by flow cytometry after staining with Annexin V and 7AAD. To further evaluate the ROS scavenging capacity of PDAB in vivo, synovial fluid was obtained via capillary puncture of the ankle joint cavity in PDAB + NIR-treated mice following sacrifice at the experimental endpoint. Malondialdehyde (MDA) levels in synovial fluid across treatment groups were quantified colorimetrically using a commercial MDA assay kit for comparative analysis. PBS-treated and PDAB-treated groups served as control cohorts.

2.7. RA model establishment and treatment

An AIA model was developed in 8-week-old adult females 18–20 g Balb/c (Changchun Yisi Experimental Animal Technology Co., Ltd., 0102171152593802), of which the protocol were reviewed and approved by Ethic Committee of Experimental Animal Ethics Committee of Jilin University (Number of permit:2024542). Initial immunization was completed using a subcutaneous injection of complete Fuchs adjuvant. On day 8, complete Fuchs' adjuvant was injected within the right hind foot pad.

To enable in vivo tracking, a 20 μL aliquot of PDAB-RB solution (100 μg/mL) was intra-articularly administered, followed by prompt delivery of NIR irradiation (1 W/cm^2, 5 min). Whole-body fluorescence imaging was performed using a small animal in vivo imaging system with excitation at 554 nm (λ_{ex}) and emission at 577 nm (λ_{em}). Longitudinal image acquisition was systematically conducted at predetermined timepoints, with comprehensive recording of imaging datasets. Treatments started on day 15, with injections of PBS, PDA, or PDAB solutions into the ankle joint cavity, followed by immediate NIR irradiation for the NIR groups. Treatments were administered every three days.

2.8. Clinical scoring criteria of Doppler ultrasound

Doppler ultrasound was introduced to measure joint blood flow. The scoring criteria are as follows: Level 0: No color Doppler blood flow signal within the joint; Level 1: Up to 3 color blood flow signals detected within the joint; Level 2: The color blood flow signal is more than level 1, but the blood flow filling area is less than 50 % of the joint area; Level 3: Blood flow signal distribution exceeds 50 % of the joint intra-articular area, which may manifest as reticular blood flow signal.

2.9. Measurement of paw withdrawal latency and mechanical withdrawal threshold

Paw withdrawal latency reflected thermal sensitivity was assessed using a hot plate set at 52.5 °C. After 30 min ambient-temperature acclimation, mice were placed on the heated surface. Latency to pain response (paw lift, lick, or jump) was recorded with a 30 s cutoff to prevent tissue damage. Three measurements per mouse were obtained at 15 min intervals.

Mechanical withdrawal threshold reflected mechanical sensitivity was quantified using von Frey filaments applied vertically to the plantar surface of the right hind paw. Beginning with a 0.6 g filament (1–2 s

application), responses were recorded as positive (paw withdrawal/licking, denoted "X") or negative (no response, "○"). Filament strength was adjusted downward after positive responses and upward after negative responses. Testing continued until stable thresholds were established (typically 5 trials), with the 50 % mechanical withdrawal threshold calculated using validated up-down methodology via dedicated software.

2.10. Spinal cord and dorsal root ganglia immunofluorescent staining

After mice were anesthetized with isoflurane by inhalation, they were perfused with physiological saline and 4 % paraformaldehyde, respectively. The L3-5 spinal cord segments at the lumbosacral expansion of mice were dissected out, dehydrated by sucrose gradient, and cryosectioned. Following antigen retrieval, sections were blocked and sequentially incubated with primary antibodies against c-Fos, TRPV1, and NeuN. After washing to remove unbound antibodies, fluorophore-conjugated secondary antibodies were applied for target detection. The nuclei were stained and sealed, and the fluorescent signals were observed using a Leica fluorescence microscope to analyze the expression and distribution. The number of positive neurons were calculated with Image J.

2.11. Histochemical staining and histochemistry analysis

Following euthanasia, hearts, livers, spleens, lungs, kidneys, and right ankle joints were harvested and fixed in 4 % paraformaldehyde. Vital organs underwent paraffin embedding, sectioning, and hematoxylin-eosin (H&E) staining for nanomaterial biosafety evaluation. Right ankle joints were decalcified in 10 % EDTA at 37 °C for 4 weeks. Post-decalcification specimens were paraffin-embedded, sectioned, and stained with both H&E and Safranin O-Fast Green to assess articular closure extent.

Immunohistochemical detection was performed for determining the expression of MMP-13 (1:100), TNF-6 (1:100), and CD31 (1:250) in ankle joints, as well as the expression of IL-1β (1:100), TNF-α (1:100), CD68 (1:100), and Iba-1 (1:200) in spinal cord tissue. Sections underwent sequential incubation with primary antibodies followed by HRP-conjugated secondary antibodies. Diaminobenzidine chromogenic development proceeded with hematoxylin counterstaining. Stained sections were imaged using a ZEISS microscope system.

2.12. Western blot analysis

Following euthanasia at the experimental endpoint, L3-L5 spinal cord segments were harvested from Naive, PBS, PDA, PDAB, and PDAB + NIR treatment groups. Tissue specimens were homogenized in lysis buffer, sonicated, and centrifuged to collect supernatants. Total protein concentration was determined by BCA assay with subsequent normalization to uniform concentration and denaturation in boiling water bath. Denatured proteins (30 μg per lane) were resolved via 10 % SDS-PAGE under two-stage electrophoresis: 80 V constant voltage for 30 min followed by 120 V for 60 min. Proteins were electrophoretically transferred to PVDF membranes using wet transfer methodology (300 mA constant current, 90 min), then blocked with 5 % non-fat milk at room temperature for 1 h. Membranes were incubated overnight at 4 °C with shaking in primary antibodies specific for: phospho-NF-κB p65 (Ser276) (1:1000), total NF-κB p65 (1:1000), and β-actin loading control (1:5000). After incubation with HRP-conjugated secondary antibody (1:5000, room temperature, 1 h), protein bands were visualized by ECL chemiluminescence. Band intensity quantification was performed using ImageJ software, with phospho-p65/total p65 ratios calculated to quantitatively evaluate the inhibitory effect of PDAB + NIR treatment on NF-κB p65 phosphorylation.

2.13. Statistical analysis

All values were represented as the mean ± standard deviation. The significance between groups was assessed using a twotailed Student's *t*-test. A p value was less than 0.05 was considered a statistically significant difference.

3. Results and discussion

3.1. Synthesis and characterization of PDAB

Typical wet chemical synthesis methods helped prepare PDA nanospheres, and AB was added at the final stage of dopamine self-polymerization to form PDAB nanocomposites through hydrogen bonding. Transmission electron microscopy (TEM) images indicated that PDAB were spherical nanostructures with diameter of about 200 nm (Fig. 1A). The potential of PDA decreased from −16.2 to −24.9 mV after loading AB (Fig. 1B), suggesting successful synthesis of PDAB. Furthermore, the hemolysis assay of PDAB was carried out to explore its biocompatibility. As shown in Fig. 1D, the hemolysis rate was maintained within 1 % even the concentration increased to 400 μg/mL, demonstrating the good stability and biocompatibility. The photothermal effect of PDAB was examined upon an 808 nm laser irradiation using an infrared thermometer. It was clear that the aqueous solution of PDAB (100 μg/mL) displayed NIR-photothermal effect, and the temperature rose with increased PDAB concentration and NIR power density (Fig. 1C–S1). In addition, PDAB also exhibited good photothermal stability upon four consecutive on/off cycles of laser irradiation (Fig. S2). To protect normal cells and tissues from hyperthermia, we selected 1W/cm^2 as the optimal power intensity of NIR laser when the temperature of PDAB solution (100 μg/mL) was below 39 °C. We evaluated the cytotoxicity of PDAB towards C17.2 and L929 cells using the CCK-8 kit, and almost no toxicity could be observed in the concentration range of 3–200 μg/mL within 24 and 48 h (Fig. 1E–S3). Even exposed to NIR irradiation (1W/cm^2, 5 min), no significant cytotoxicity generated when the concentration of PDAB reached 100 μg/mL (Fig. 1F), which was in agreement with the results of live-dead cell staining assay (Fig. S4). The above data guarantees the biosafety of the treatment that combines PDAB and low-power NIR irradiation.

3.2. Dual-responsive H_2 production and bioreduction capacity

As a commonly used hydrogen-generating material, AB offers substantial advantages including high mass storage capacity (19.6 wt%), ambient stability, mild hydrolysis conditions and controllable hydrogen release [26]. While minimally reactive with water at room temperature, AB undergoes rapid hydrolysis in the acidic microenvironment of rheumatoid arthritis (RA) joints (pH 4.7–6.8) [27]. Fig. 1G presents real-time visualization of hydrogen bubble dynamics in the PDAB + NIR group, showing a gradual increase in bubble number over time (Fig. S5). Further quantitative analysis using a hydrogen concentration tester revealed that PDAB's hydrogen production rate increased under acidic conditions and accelerated further with NIR irradiation (Fig. 1H). Compared with PDAB solution at pH of 5, applying NIR irradiation for 10 min could increase the H_2 production rate by 28 %. NIR irradiation elevates the interfacial temperature through the photothermal effect of PDA, accelerating the protonation attack of H^+ on the B–N bond. Simultaneously, the intrinsic quinone/phenol redox couple of PDA directly catalyzes the hydrolysis of B-H bonds. These dual effects synergistically enable efficient hydrogen generation under metal-free conditions. This strategy enables on-demand and efficient hydrogen release, offering a new perspective for the design of safe hydrogen storage materials.

Prior to bioreductive detection, L929 cellular uptake of PDAB was monitored via RB labeling for subcellular localization. Confocal microscopy revealed distinct intracellular RB signals within 1 h of incubation,

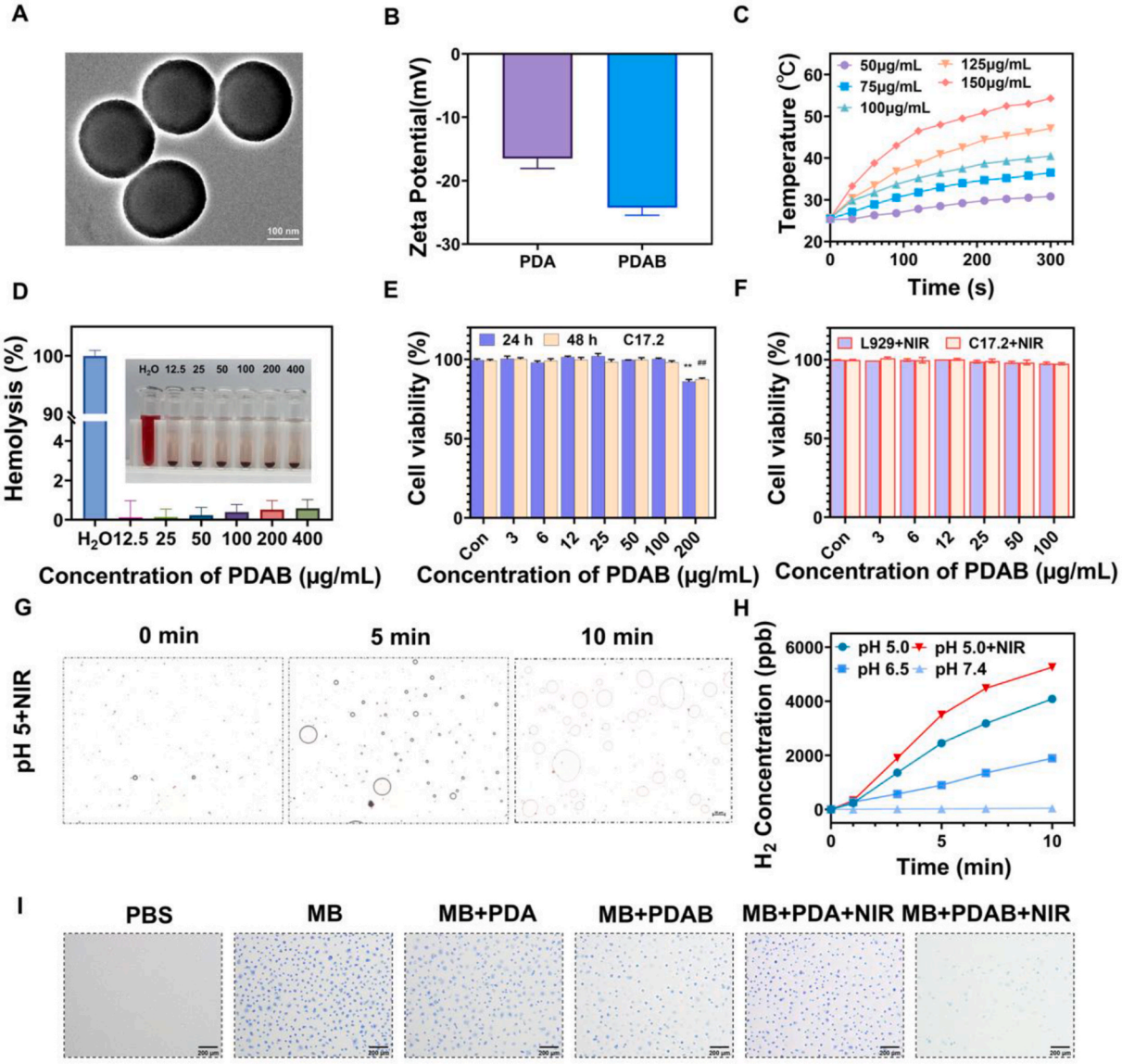

Fig. 1. PDAB characterization. (A) TEM images of PDAB. (B) Zeta potential of PDA and PDAB. (C) Photothermal curves of PDAB (100 μg/mL) irradiated with varying powers of NIR laser. (D) The hemolysis rate of PDAB with different concentrations. (E) Viabilities of C17.2 cells cells treated by PDAB for 24 and 48 h. Data are expressed as mean ± SD (n = 4). Statistical significance was assessed by a twotailed Student's *t*-test, $^{**}p < 0.01$,$^{\#\#}p < 0.01$. (F) Viabilities of L929 and C17.2 cells cells treated by PDAB with NIR irradiation (1W/cm^2, 5 min). (G) Photomicrographs of H_2 bubbles generated from PDAB under different pH and NIR irradiation. (H) Dynamic changes of produced H_2 level corresponding to Fig. 1G. (I) Photo of color change of methyl blue-stained C17.2 cells with different treatments.

with red fluorescence intensity progressively increasing over time. This temporal enhancement demonstrates continuous internalization of PDAB by the cells (Fig. S6). The bio-reductivity of PDAB was further evaluated in C17.2 cell model via MB probe. As shown in Fig. 1I, there is no apparent fading phenomenon in the hydrogen-free group, while the PDAB group showed slight fading. Following NIR irradiation, hydrogen evolution accelerated, and the cell fading becomes more pronounced. The corresponding quantitative analysis of residual MB through an enzyme marker was in agreement with the fading of cells (Fig. S7). Therefore, PDAB exhibited dual responsiveness to acidic environments and NIR irradiation, and the generated hydrogen exhibited biological reducibility.

3.3. PDAB-mediated ROS scavenging reverses oxidative apoptosis in C17.2 cells

High levels of ROS lead to joint damage and inflammation, and are closely related to intensified pain in RA sufferers. The demonstrated bioreducibility inspires us to continue exploring the ROS scavenging ability of PDAB through the utilization of H_2O_2 as an inducer of oxidative stress and the DCFH-DA probe for the detection of intracellular ROS levels (Fig. 2A). The structure of PDA encompasses abundant phenolic hydroxyl groups that possess antioxidant activity, and these phenolic hydroxyl groups are capable of neutralizing ROS by donating hydrogen atoms [28]. Consequently, the PDA carrier can collaborate with hydrogen to exert its function in scavenging ROS. In comparison with the H_2O_2 group, the fluorescence was attenuated within all treatment groups. As determined by flow cytometric analysis, the mean fluorescence intensity (MFI) in the PDA group was found to be 31-fold lower than that of the H_2O_2 group (Fig. 2B). Moreover, the introduction of hydrogen further diminished the level of ROS by 4 folds. Notwithstanding the fact that we have maintained the temperature below 40 °C, the ROS level in the PDA + NIR group was substantially elevated on account of the photothermal effect of PDA. When PDA is supplanted by PDAB, NIR irradiation expedites the release of H_2, and the local high-level H_2 effectively counteracts the elevation of intracellular ROS

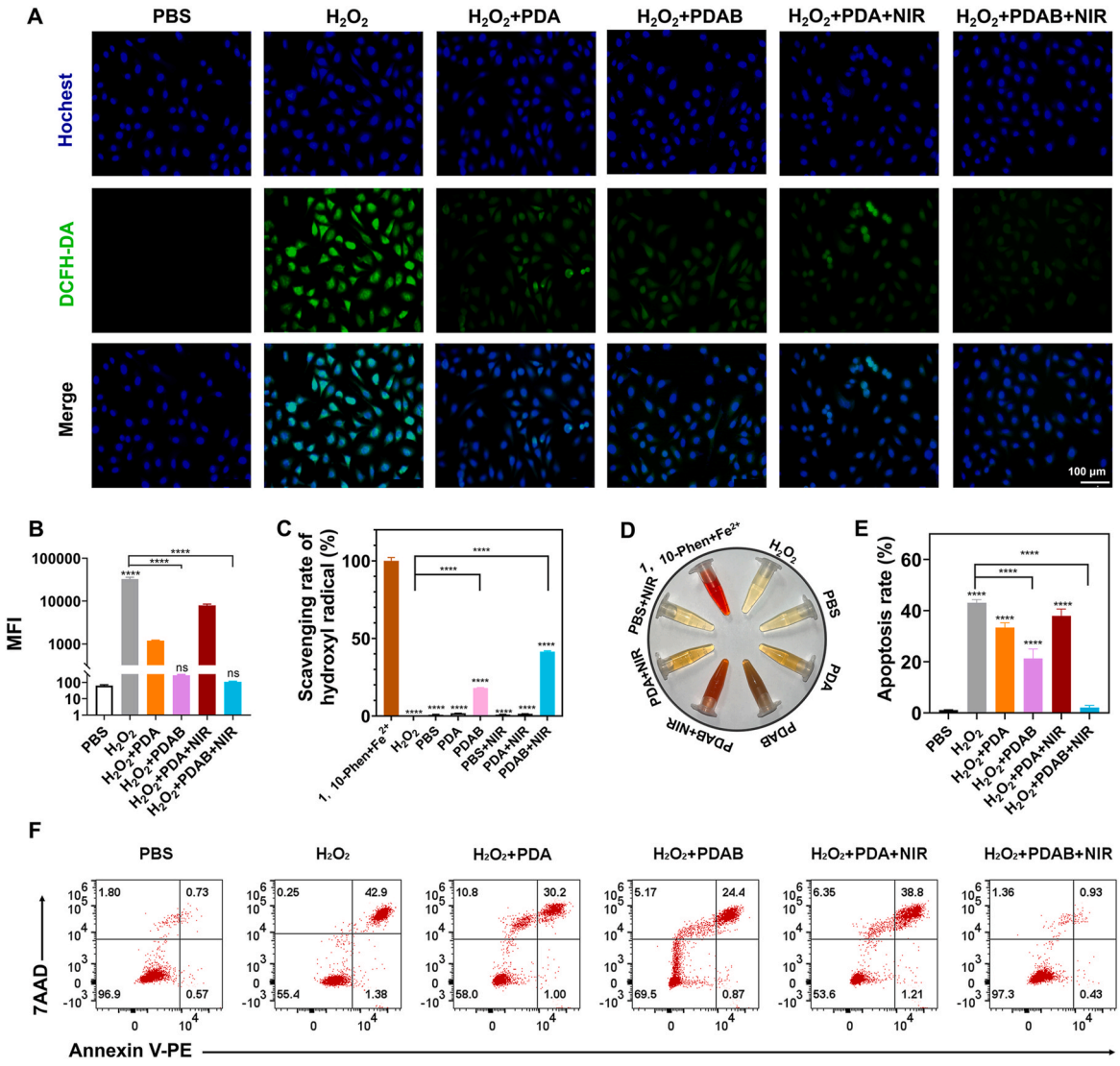

Fig. 2. *In vitro* ROS scavenging ability of PDAB. (A) Representative images of ROS staining in L929 cells under different treatments. (B) Quantitative analysis of mean fluorescence intensity of L929 cells in Fig. 2A (n = 4). (C) Quantitative analysis of ·OH scavenging rate in different groups. Data are expressed as mean ± SD (n = 4). Statistical significance was assessed by a twotailed Student's *t*-test, ****p < 0.0001. (D) Color changes of mixed solution of 1,10-phenanthroline and $FeSO_4{\cdot}7H_2O$ after different treatments. (E) Quantification of cell apoptosis from the data of panel F. Data are expressed as mean ± SD (n = 3). Statistical significance was assessed by a twotailed Student's *t*-test, ****p < 0.0001. (F) Flow cytometry analysis of C17.2 cell apoptosis upon different treatments.

elicited by PTT, thereby achieving the maximal ROS removal efficiency of 99.65 %. Among various ROS, ·OH exacerbates synovial cell inflammation and causes destruction of articular cartilage and bone [29,30]. Hydrogen can selectively eliminate ·OH in the joint cavity, reducing synovial inflammation and joint pain/swelling. The combination of o-phenanthroline and ferrous ions (Fe^{2+}) forms a stable cherry-red tris (1,10-phenanthroline)iron(II) complex ($[Fe(phen)_3]^{2+}$). Subsequent introduction of hydroxyl radicals (·OH) induces ligand displacement and complex dissociation, resulting in solution bleaching (Fig. 2D). Consequently, the degree of chromogenic recovery quantitatively correlates with antioxidant scavenging efficiency toward ·OH. Under low-dose conditions, the scavenging rate of the PDAB + NIR group for ·OH is 41 % (Fig. 2C). Remarkably, this rate represents a 2.3-fold increase over the PDAB group and a 24-fold enhancement compared to the PDA group, demonstrating PDAB's intrinsic ·OH scavenging capability with significant amplification under NIR irradiation.

The scavenging of ROS is anticipated to reverse cell apoptosis. Consequently, we investigated the apoptosis of C17.2 cells treated with the aforementioned treatments by employing CCK-8 kits and flow cytometry. From flow cytometric analysis in Fig. 2E, the cells at different stages were quantitatively distinguished by dual fluorescence of Annexin V-FITC/PI. In different treatment groups, the occurrence of cell apoptosis exhibits a highly consistent trend of change with the levels of ROS. H_2O_2, a common kind of ROS endowed with remarkable oxidizing power, can shatter the intrinsic redox equilibrium within cells upon their exposure. This disruption thrusts the cells into a state of oxidative stress and inflicts damage on the integrity of mitochondrial membranes, ultimately triggering cell apoptosis. As can be seen, culturing C17.2 cells with medium containing H_2O_2 led to a significant apoptosis of C17.2 cells (42.9 %). Due to the relatively low ROS scavenging efficiency of PDA at low doses (Fig. 2E), the apoptosis rates obtained for the PDA and PDA + NIR groups were almost indistinguishable from that of pure H_2O_2 group. In contrast, the apoptosis rate dropped to 21 % in PDAB group and further decreased to 2 % in the PDAB + NIR group, attributed to the remarkable ROS scavenging capacity of hydrogen (Fig. 2E and F). In addition, cell viability measured by CCK8 assay was in line with the aforementioned findings (Fig. S8).

3.4. Remission of clinical symptoms in RA mice

To evaluate the anti-inflammatory effects, we explored the remission of clinical symptoms in RA mice through H_2-induced ROS scavenging. The RA model was established via subcutaneous injection of complete Freund's adjuvant in the groin area of BALB/c mice, which remains widely accepted for studying acute-phase joint inflammation and inflammation-mediated pain, as well as evaluating the therapy outcome in early therapeutic windows. Booster immunization was administered via injection into the right footpad 1 week post-primary immunization. The mice were randomly allocated into seven distinct groups: the naive group, the PBS group, the PBS + NIR group, the PDA group, the PDA +

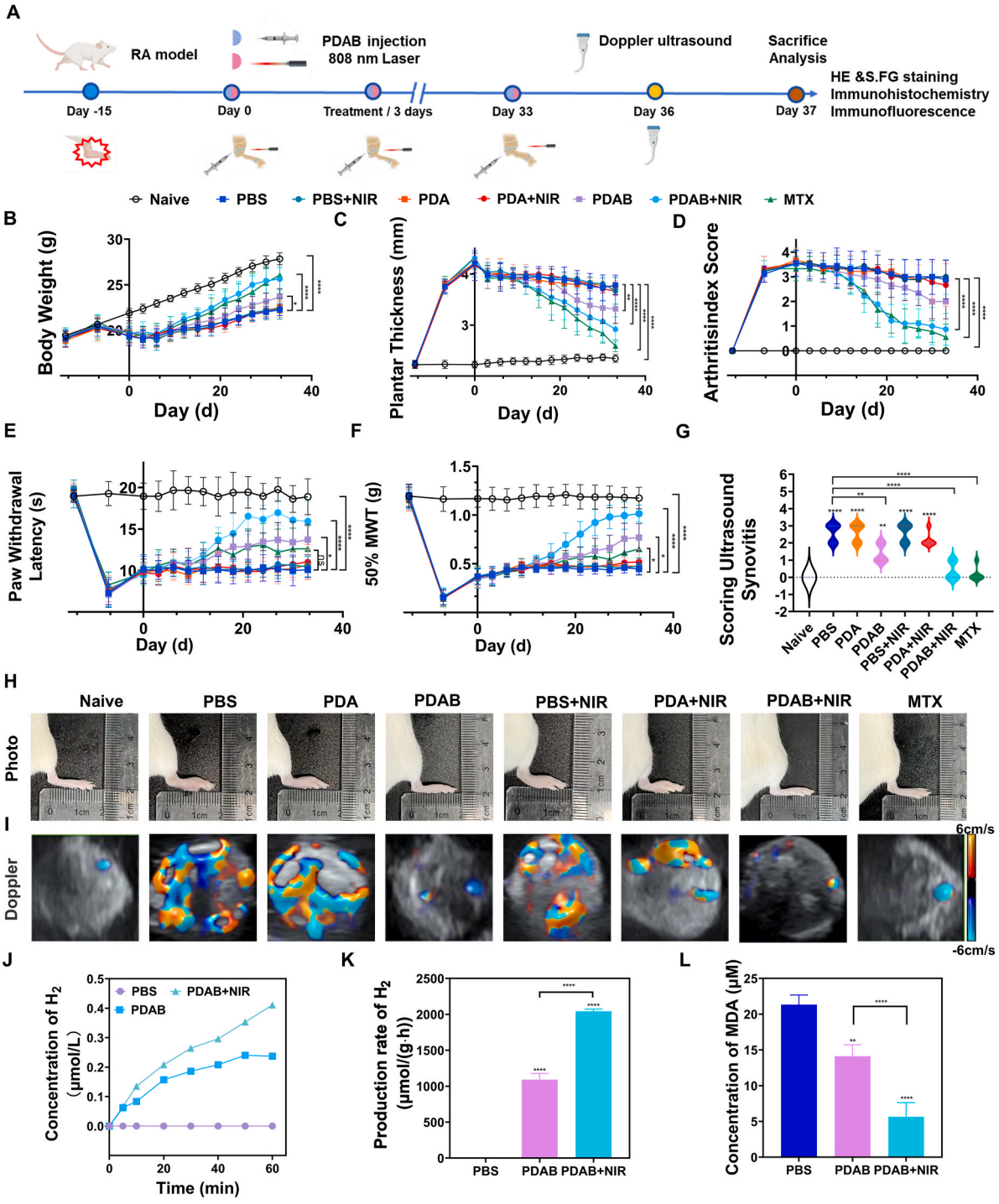

Fig. 3. *In vivo* therapeutic outcome of PDAB + NIR. (A) Schematic diagram of the experimental process of treating RA mice with PDAB + NIR. Body weight (B) and the mean paw thickness (C) and arthritis index (D) in each group were calculated every 3 days until sacrifice. (E) Statistical analysis of Paw Withdrawal Latency under various treatments. (F) Statistical analysis of 50 % Mechanical Withdrawal Threshold (50 % MWT) under various treatments. (G) Grading of synovial blood flow based on ultrasound images. (H) Representative image from macroscopic observation of the hind legs in different treatment groups. (I) Images showing Doppler ultrasound detection of changes in blood flow in the mouse ankle joint synovium. Levels (J) and rates (K) of generating H_2 in different groups. (L) MDA concentrations across treatment groups. Data are expressed as mean ± SD (Fig. 3B–F n = 9; Fig. 3K–L n = 3). Statistical significance was assessed by a twotailed Student's *t*-test. *p < 0.05, **p < 0.01, ****p < 0.0001.

NIR group, the PDAB group and the PDAB + NIR group. Prior to therapeutic regimen formulation, we characterized the in vivo biodistribution and metabolic profile of intra-articularly administered PDAB nanocomposites. The PBS control group showed no ankle fluorescence throughout the experiment, excluding interference with PDAB signals. In the PDAB + NIR group, fluorescence surged within 30 min post-injection, indicating rapid nanoparticle diffusion into synovium. Acidic joint microenvironments triggered aminoborane protonation and hydrogen release, accelerated by NIR irradiation. From 3 to 6 h, sustained hydrogen production coincided with nanoparticle migration to popliteal lymph nodes. By 12 h, nanoparticles accumulated predominantly in popliteal nodes, extending to inguinal nodes by 48 h. At 72 h, only residual fluorescence persisted in inguinal nodes, suggesting nearly complete PDA clearance. In addition, no significant fluorescence appeared in other organs, indicating the good biological safety (Fig. S9). As depicted in Fig. 3A, the treatment was initiated on the 15th day subsequent to the establishment of the RA model. Mice underwent twelve treatment sessions at 72 h intervals, aligned with PDAB's in vivo metabolic clearance profile, during which the changes in weight, foot thickness, arthritis scores and pain behavior scores were recorded. We used methotrexate (MTX), a clinically used therapeutic agent for RA, as a positive control to assess the therapeutic effects of hydrogen therapy in alleviating clinical symptoms.

The paw thickness and arthritis index scores are pivotal parameters for assessing the anti-inflammatory effect during arthritis progression, and the healthy mice without any treatment served as the normal control (Naive group). Upon examination of the paw thickness of mice underwent different treatments, an appreciable alleviation is manifested in PDAB ± NIR and MTX treatment groups. Application of NIR elevated local hydrogen concentration within the joints, enhancing ROS scavenging, mitigating inflammation, and reducing swelling. Toe thickness decreased from 3.8 mm (PDAB group) to 2.9 mm (PDAB + NIR group), while remaining marginally higher than that in the MTX group (2.6 mm) (Fig. 3C and I). Consistent with the alleviation of clinical signs, both PDAB + NIR and MTX groups exhibited the lowest arthritis scores 1 point (Fig. 3D). Rheumatoid vascular opacities are the hallmark symptoms of RA, characterized by synovial tissue hyperplasia, neovascularization, and infiltration of activated inflammatory cells, posing a substantial threat to joint integrity. Leaving untreated, this aggressive vascular opacification tends to invade adjacent structures, causing progressive and irreversible damage to bone, cartilage, tendons, and ligaments [31]. Doppler ultrasound assessment revealed distinct patterns of joint neovascularization across treatment groups (Fig. 3I). PBS-treated mice exhibited significantly elevated and irregularly distributed blood flow signals, indicating pathological angiogenesis. Conversely, both PDAB + NIR and MTX groups demonstrated signal characteristics comparable to Naive controls, featuring moderate intensity, homogeneous morphology, and reduced spatial distribution. Quantitative clinical scoring confirmed these findings that PBS specimens showed markedly increased signal intensity (>50 % total area coverage) with heterogeneous vascular patterns. In contrast, PDAB + NIR treatment yielded signals of significantly lower intensity and distribution, closely approaching physiological levels observed in both MTX and Naive groups. These results demonstrate that PDAB + NIR treatment effectively suppresses RA-induced pathological angiogenesis (Fig. 3G), mirroring the therapeutic efficacy of MTX. Further, we conducted regular von frey silk wires and hot plates tests to measure the changes in pain levels at predetermined time points set before modeling and after treatment to evaluate the analgesic effect of hydrogen therapy and MTX treatment. In comparison to Naive group, the paw retraction threshold/reaction time of RA mice in all groups before treatment was at a relatively low level on the 7th day subsequent to injection with complete Freund's adjuvant. Additionally, a slight increase was observed before treatment, which could be attributed to the transition from local inflammation at the foot pad injection site to joint inflammation. Consequently, the pain levels in our RA model were similar across all groups prior to treatment. Upon 12 treatments with an interval of 3 days, no analgesia including mechanical pain and thermal pain was detected within the thermotherapy group. The analgesic effect of MTX treatment was marginally lower than that of PDAB treatment and significantly lower than that of PDAB combined with NIR (Fig. 3E and F). Notably, MTX has demonstrated superior anti-inflammatory efficacy compared to the PDAB-based hydrogen therapy, whereas limited analgesic efficacy. This observed decoupling effect between inflammation alleviation and pain relief during RA treatment demonstrates the superior therapeutic potential of molecular hydrogen over conventional anti-inflammatory agents in comprehensive RA management. Consistent with reduced disease burden, PDAB + NIR and MTX groups exhibited significantly greater weight gain compared to PBS controls, approaching Naive levels (Fig. 3B). Consequently, subsequent investigations will prioritize elucidating the mechanisms underpinning H_2 therapy in concurrently modulating anti-inflammatory and analgesic responses.

To establish a causal link between H_2-mediated antioxidant effects and symptom improvement, we measured H_2 concentration and MDA levels in joint lavage fluid from mice in each treatment group. The results demonstrated that PDAB effectively releases hydrogen and scavenges ROS at the joint site, thereby alleviating inflammation and producing analgesic effects. Hydrogen production was quantified through MB reduction assays. As shown in Fig. 3J, hydrogen molecules generation kinetics of PDAB + NIR group ensures stable and sustained hydrogen release in joint lavage fluid and reveals NIR-triggered hydrogen generation compared to PDAB alone. Quantitative production rate analysis (Fig. 3K) further established that PDAB + NIR generated hydrogen at rates notably exceeding PDAB alone (1.87 folds). These data collectively demonstrate that NIR irradiation is essential for robust hydrogen evolution from PDAB in simulated arthritic microenvironments. As the terminal product of lipid peroxidation, MDA accumulation positively correlates with prior ROS exposure and offers greater detection convenience than direct measurement of short-lived ROS species, establishing it as the gold standard biomarker for oxidative stress assessment. We further measured MDA levels across treatment groups to evaluate in vivo ROS scavenging efficiency of hydrogen therapy. Consistent with hydrogen quantification data, the PDAB group exhibited 66.3 % reduction in MDA concentration compared to PBS controls. NIR application elevated local hydrogen concentration, further reducing MDA levels to 26.6 % (Fig. 3L), demonstrating enhanced antioxidant capacity. These data compellingly demonstrate that hydrogen significantly enhances the clinical outcomes by relieving joint swelling and inhibiting the growth of vascular opacities through the scavenging of local ROS in RA.

3.5. The progression inhibition of RA in mice

Cartilage destruction represents an important feature of RA and serves as a sign of disease progression, which is associated with an elevated risk of joint deformity and long-term disability. Preventing or decelerating cartilage destruction constitutes a primary objective of RA treatment to mitigate long-term complications and enhance the patient's quality of life. The protection of cartilage is a crucial factor in guiding treatment decisions. The protective effect of hydrogen on cartilage was evaluated using H&E and S/O staining. On the 48th day after modeling, the cartilage surface of the mice in the PBS group exhibited defects due to inflammatory erosion, and the thickness of the cartilage matrix was reduced. In contrast, the treatment with PDAB + NIR significantly mitigated the loss of both cartilage and cartilage matrix. The articular cartilage surface was smooth and structurally intact, and cartilage content increased from 24 % to 59 % (Fig. 4A, B, F), suggesting that hydrogen can effectively alleviate cartilage damage, thereby restraining RA. Matrix metalloproteinase-13 (MMP-13), a matrix metalloproteinase, exhibits the remarkable capability of degrading multiple types of collagen proteins, with particular emphasis placed on type II collagen which constitutes a major component of cartilage, which is

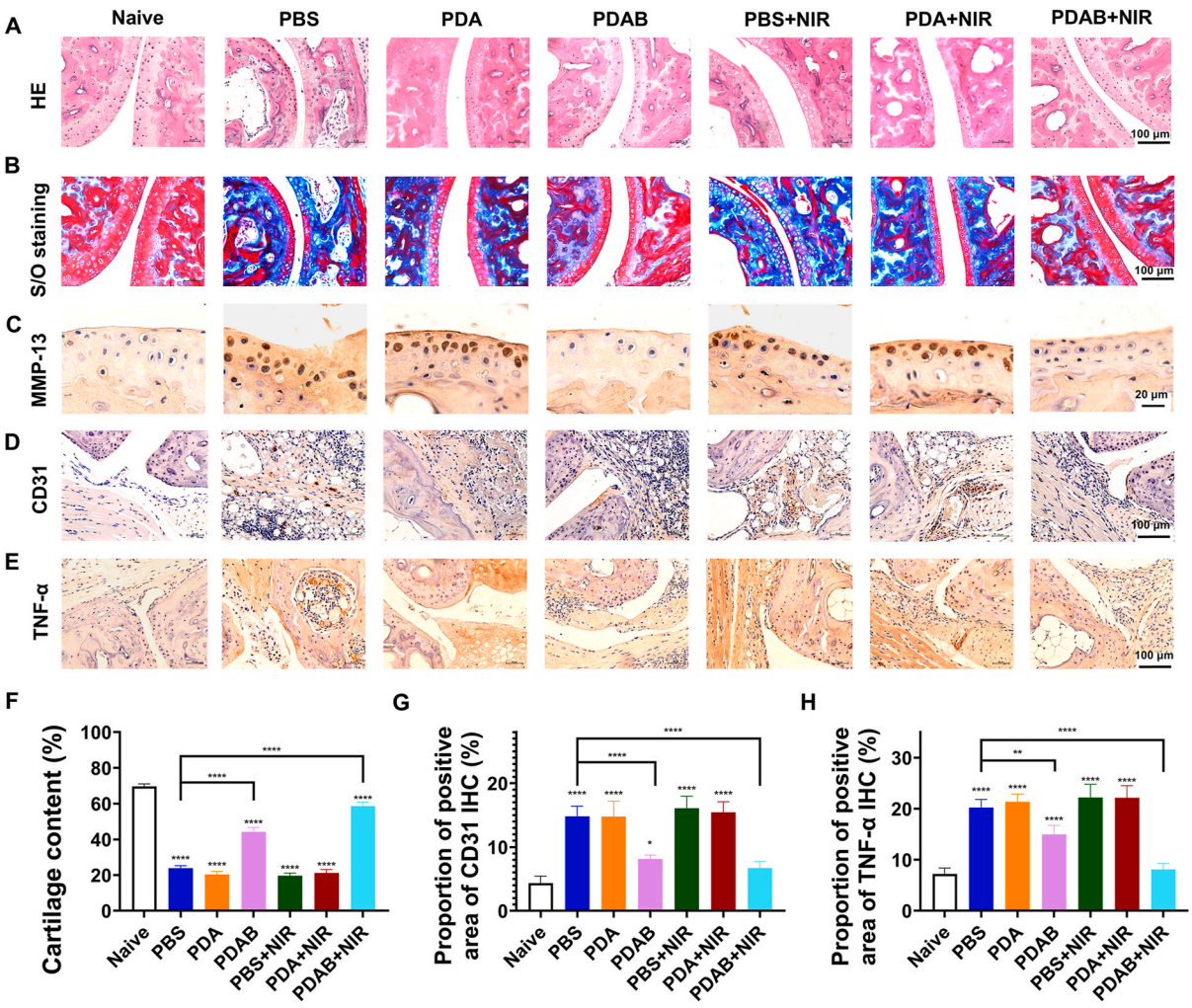

Fig. 4. Attenuation of joint destruction. (A) H&E and (B) Safranin-O staining of RA mice with different treatments. Immunohistochemistry of the expressions of MMP13 (C), CD31 (D) and TNF-α (E) in extracellular cartilage matrix of RA mice in different groups. The percentages of cartilage content (F), CD31 (G) and TNF-α (H) positive chondrocytes (n = 3). Data are expressed as mean ± SD (n = 5). Statistical significance was assessed by a twotailed Student's *t*-test. *p < 0.05, **p < 0.01, ****p < 0.0001.

pivotal in the cartilage destruction process within RA [32]. Lowering the expression level of MMP-13 can decelerate the advancement of RA. Immunohistochemical staining revealed significantly reduced MMP-13 expression in articular cartilage following PDAB + NIR treatment compared to other groups (Fig. 4C). While PDAB monotherapy moderately decreased MMP-13 levels, its efficacy was substantially lower than the combined intervention. These results demonstrate hydrogen-mediated inhibition of MMP-13 expression, which escalates with locally elevated hydrogen concentrations. Furthermore, expression of CD31 (cluster of differentiation 31), an established angiogenesis marker, was significantly attenuated in periarticular tissues of the PDAB + NIR group versus PBS controls (Fig. 4D–G). The diminished neovascularization would signify an inhibitory impact on the growth of vascular opacities, which matched well with the results of Doppler ultrasound. Tumor necrosis factor-alpha (TNF-α), a crucial pro-inflammatory factor within the inflammatory response, facilitates the initiation and progression of inflammation via multiple pathways. Decreased TNF-α expression or activity serves as a clinically significant biomarker for inflammation alleviation. As shown in Fig. 4E, TNF-α positive areas were significantly intensified in hydrogen free groups. Conversely, TNF-α positive areas were reduced after PDAB treatment, and the percentage of TNF-α positive chondrocytes in the PDAB + NIR group was 1.75 folds lower than that of PDAB group (Fig. 4H), evidencing the anti-inflammatory activity of gaseous hydrogen. Collectively, these data demonstrate that in-situ-generated high--concentration hydrogen gas exerts potent anti-inflammatory effects, inhibiting cartilage matrix degradation and modifying disease progression in RA.

3.6. Pain relief analysis

In chronic pain states, nociceptive stimulation induces sequential activation of neurons within DRG and the spinal dorsal horn, thereby eliciting central sensitization and augmenting thermal nociceptive sensitization, ultimately leading to the formation of pain sensations in the cortex [33]. The transient receptor potential vanilloid (TRPV), which is predominantly distributed on injured neurons, has been implicated in various pain states, including inflammatory pain and hyperalgesia, through the activation of the TRPV1 channel [34,35]. The expression of C-fos is upregulated in response to enhanced neuronal activity and has emerged as a reliable indicator of pain signaling and processing [36,37]. Cells in DRG displaying co-localized expression of these two proteins are characterized as activated positive neuronal cells. NeuN is a neuron-specific nuclear protein, which is a specific marker of neurons [38]. Neurons expressing NeuN and C-fos in the dorsal horn of the spinal cord are considered to be in an activated state, participating in the signal conduction and regulation of chronic pain [39]. We performed immunofluorescent staining for L3-5 DRGs and the dorsal horn

region of the spinal cord after treatment to analyze the activation status of neurons. As depicted in Fig. 5A, the proportion of double-positive cells of c-Fos and TRPV1 in the naive group at the DRG location is merely 23 %. After modeling, the ratio of positive cells in the PBS group increased to 64 %, which was subsequently reduced to 24 % upon PDAB + NIR treatment, nearly equivalent to that of the Naive group (Fig. S10). In a similar vein, 29 % of neurons were activated in the SG region of the spinal cord's dorsal horn in the PBS group due to the inflammatory signaling and persistent nociceptive input, and the neuron activation in RA mice undergoing PDA ± NIR treatment was not significantly restrained. In contrast, only 12 % and 8.9 % of neurons were activated within the PDAB and PDAB + NIR groups, respectively (Fig. 5B–S11). The aforementioned results suggest that hydrogen could effectively suppress pain-related neuron activation, thereby reducing central sensitization.

3.7. Hydrogen reducing central sensitization of dorsal horn neurons by scavenging ROS

Prior studies demonstrate that molecular hydrogen effectively scavenges ROS, thereby preserving mitochondrial function and suppressing ROS bursts in neurons [40,41]. Given that ROS is a classical activator of the NF-κB pathway, hydrogen administration attenuates nuclear translocation of NF-κB and suppresses the production of c-Fos and IL-1β through ROS scavenging, consequently inhibiting central sensitization.

First, we investigated the mitochondrial function of C17.2 cells in different treatment groups by staining the mitochondrial membrane potential (MMP). As depicted in Fig. 6B, the mitochondria of C17.2 cells in the Naive group functioned normally, and the field of view showed a large area of red fluorescence. In contrast, green fluorescence occupied the entire field of view upon H_2O_2 treatment, as ·OH transferred from H_2O_2 severely damaged the mitochondrial function. Obviously, the introduction of PDAB effectively scavenged the generated ·OH, and the proportion of red fluorescence regained its dominance. Additionally,

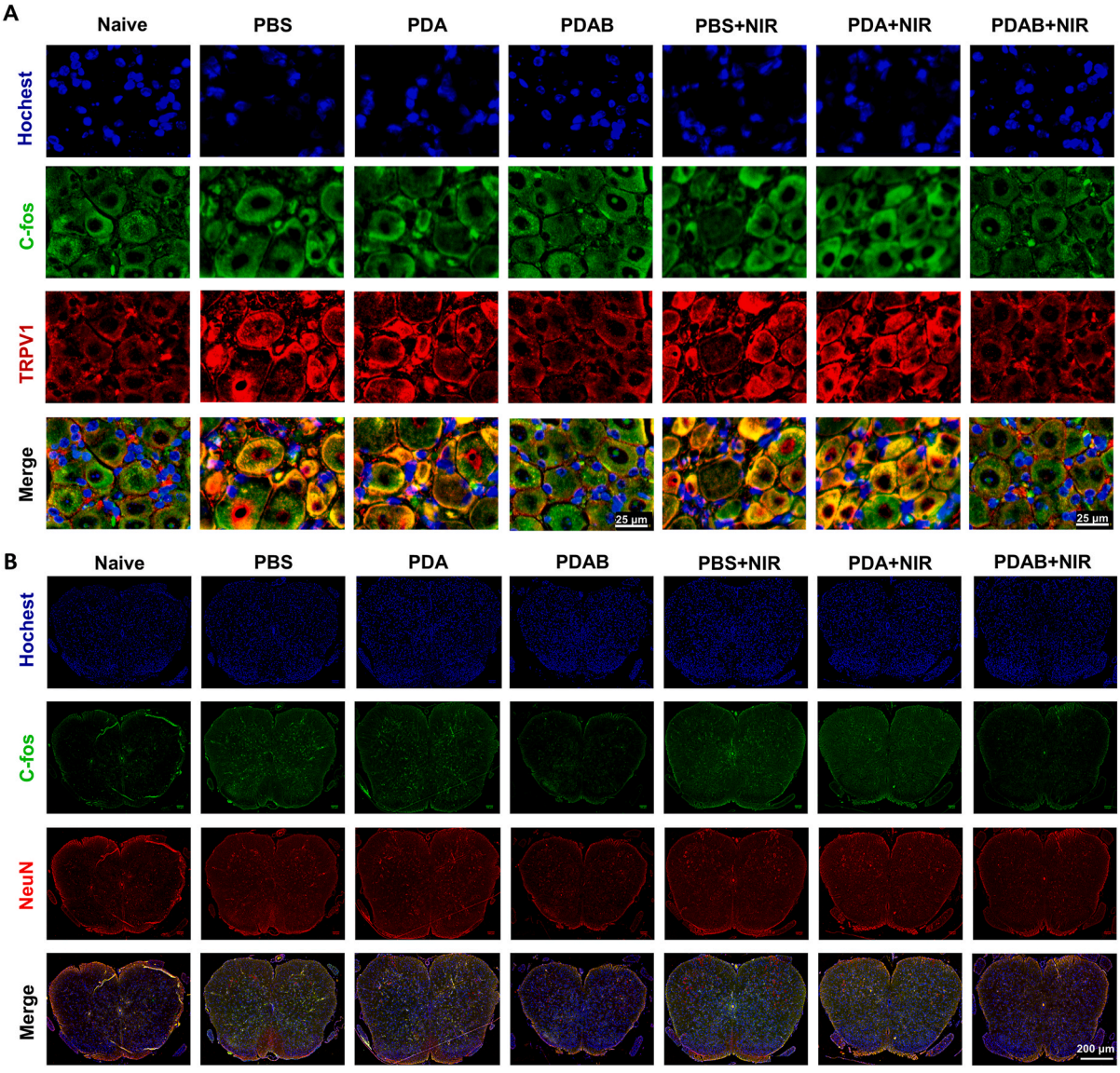

Fig. 5. Evaluation of analgesic effect of PDAB + NIR treatment. (A) Representative immunofluorescence of c-Fos and TRPV1 in DRG. Green: c-Fos$^+$, Red: TRPV1$^+$, Blue: Hochest$^+$, Yellow: c-Fos$^+$TRPV1$^+$. (B) Immunofluorescence of c-Fos and NeuN in SG area of spinal cord dorsal horn neurons. Green: c-Fos$^+$, Red: NeuN$^+$, Blue: Hochest$^+$, Yellow: c-Fos + NeuN$^+$. Data are expressed as mean ± SD (n = 9). Statistical significance was assessed by a twotailed Student's *t*-test. *p < 0.05, ****p < 0.0001.

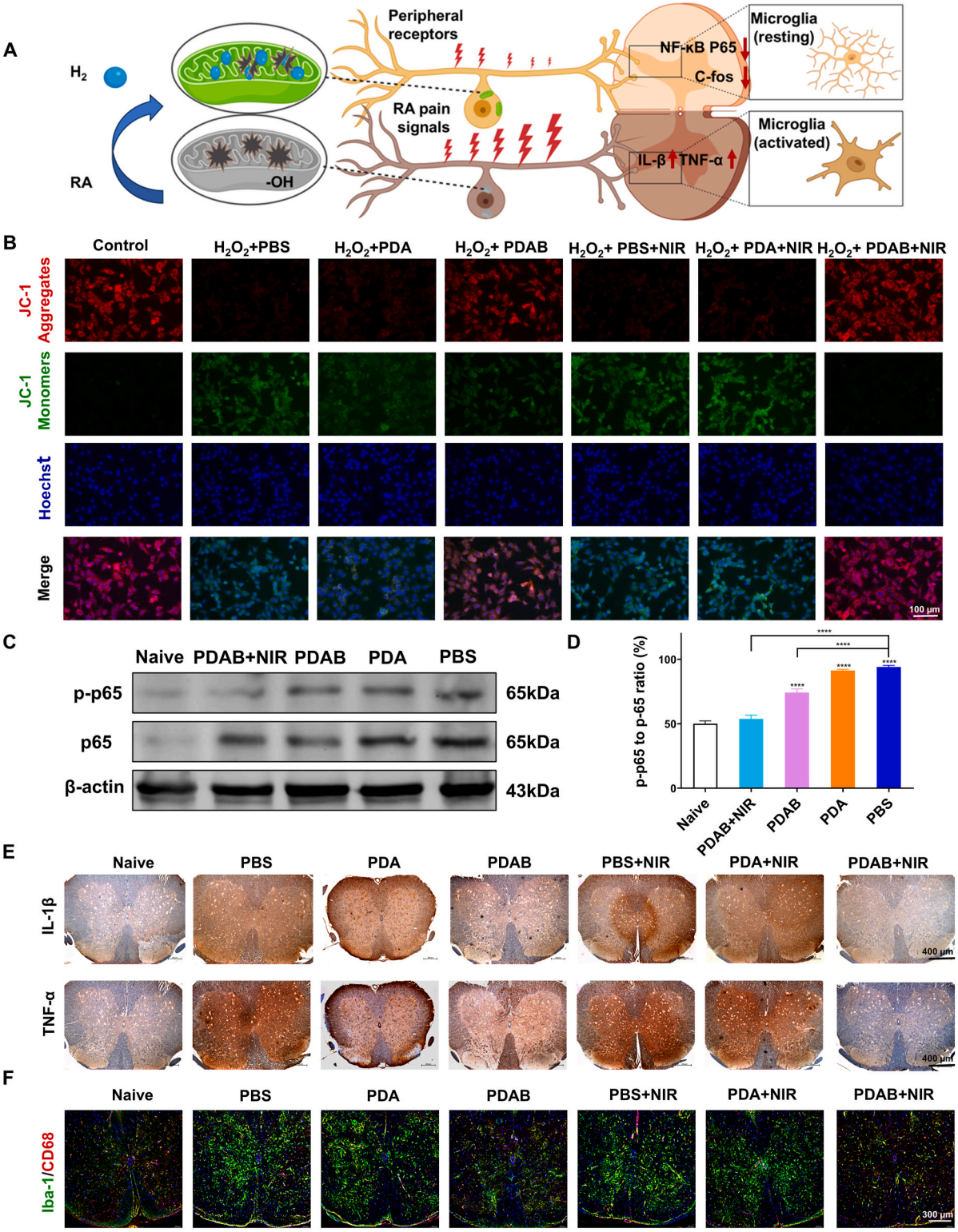

Fig. 6. (A) The schematic shows that PDAB inhibits RA pain by producing hydrogen to protect neuronal mitochondrial function and reduce the transmission of pain signals from peripheral receptors to higher nerve centers. (B) Representative immunofluorescence images of JC-1 monomers and aggregates. (C) Western blotting measured the nuclear and total NF-κB levels in the indicated groups (n = 6). (D) Analysis of p-p65 to p65 ratio (n = 3). (E) Characteristic photos of immunohistochemical staining of IL-1β and TNF-α in spinal cord tissue. (F) Iba-1 and CD68 immunofluorescence staining is used to mark activated microglia. Statistical significance was assessed by a twotailed Student's *t*-test. *p < 0.05, **p < 0.01, ****p < 0.0001.

upon NIR irradiation, the local hydrogen level was further elevated, and the removal of ·OH was even more thorough. The obtained mitochondrial membrane potential was comparable to that of the Naive group (Fig. 6B–S12). The ineffectiveness of the hydrogen-free treatment group illustrates the protective effect of hydrogen on mitochondrial function, which is consistent with the inhibition of nerve cell apoptosis by hydrogen observed in vitro experiments.

Subsequently, we assessed the inhibitory effect of hydrogen on the

NF-κB pathway in the spinal cord of RA model mice via Western blot analysis. Results demonstrated a significant increase in phosphorylation levels of NF-κB P65 in the L3-L5 spinal cord segments in the PBS control group, indicating activation of the NF-κB pathway. In contrast, mice treated with PDAB + NIR exhibited markedly reduced P65 phosphorylation levels compared to the PBS group, approaching or restoring to baseline levels. Finally, central sensitization in RA mice was evaluated by quantifying the release of inflammatory mediators and assessing microglial activation status. IL-1βand TNF-α can enhance the excitability of nociceptive neurons of the spinal cord to induce central sensitization and promote the development of inflammatory pain [42,43]. We performed immunohistochemical staining of spinal cord tissue samples from RA mice in each group, and the levels of IL-1β, TNF-α were analyzed (Fig. 6C). Compared to the overexpression of IL-1β and TNF-α at the spinal medulla site in the PBS ± NIR and PDA ± NIR groups, the groups treated with PDAB ± NIR exhibited lower levels of IL-1β and TNF-α (Fig. S13 and S14), which especially, the levels of the two inflammatory factors in the NIR group decreased more significantly. This result is also consistent with hydrogen-inhibited activation of spinal cord neuronal observed in Fig. 5C–D above, indicative of the anti-inflammation of hydrogen. We can reasonably infer that PDAB + NIR treatment reduces central sensitization by inhibiting the expression of IL-1β and TNF-α in the spinal cord of RA mice. The expression of inflammatory factors indicates the activation status of microglia, which is closely related to enhanced pain signalling. Accordingly, we also conducted immunofluorescence staining of microglia markers to visualize the inhibition of microglia activation by hydrogen therapy. Co-staining of the ionic calcium-binding ligand 1 (Iba1) and the CD68 marker facilitated the observation of the distribution, morphology, and number of activated microglia [44]. As anticipated, PDAB + NIR treatment led to a significant suppression of microglia activation, approaching the levels seen in the Naive group (Fig. 6D–S15). Based on the results of pain behavioral tests and phosphorylation levels of NF-κB, along with the expression levels of inflammatory factors and markers of central sensitization, we demonstrates that hydrogen-induced inhibition of central sensitization was achieved by regulating ROS/NF-κB pathway.

3.8. *Biosafety assessment of PDAB*

In vivo biosafety of PDA and PDAB NPs was comprehensively evaluated by performing H&E staining on major organs, specifically the hearts, livers, spleens, lungs, and kidneys of the mice. In comparison to the Naive group, neither PDA NPs nor PDAB NPs induced evident tissue damage, thus ensuring the biosafety of the proposed treatment strategy that combines PDAB with NIR irradiation (Fig. 7A). Furthermore, liver and kidney functions were systematically evaluated by detecting blood biochemical parameters, including AST (aspartate aminotransferase), ALT (alanine aminotransferase), CRE (creatinine), and BUN (blood urea nitrogen). When compared with the Naive group, the obtained serum levels of the aforementioned parameters were consistently maintained within the normal ranges (Fig. 7B). Taken together, the intra-articular injection of PDAB upon NIR irradiation at the current therapeutic dose can be considered biologically safe.

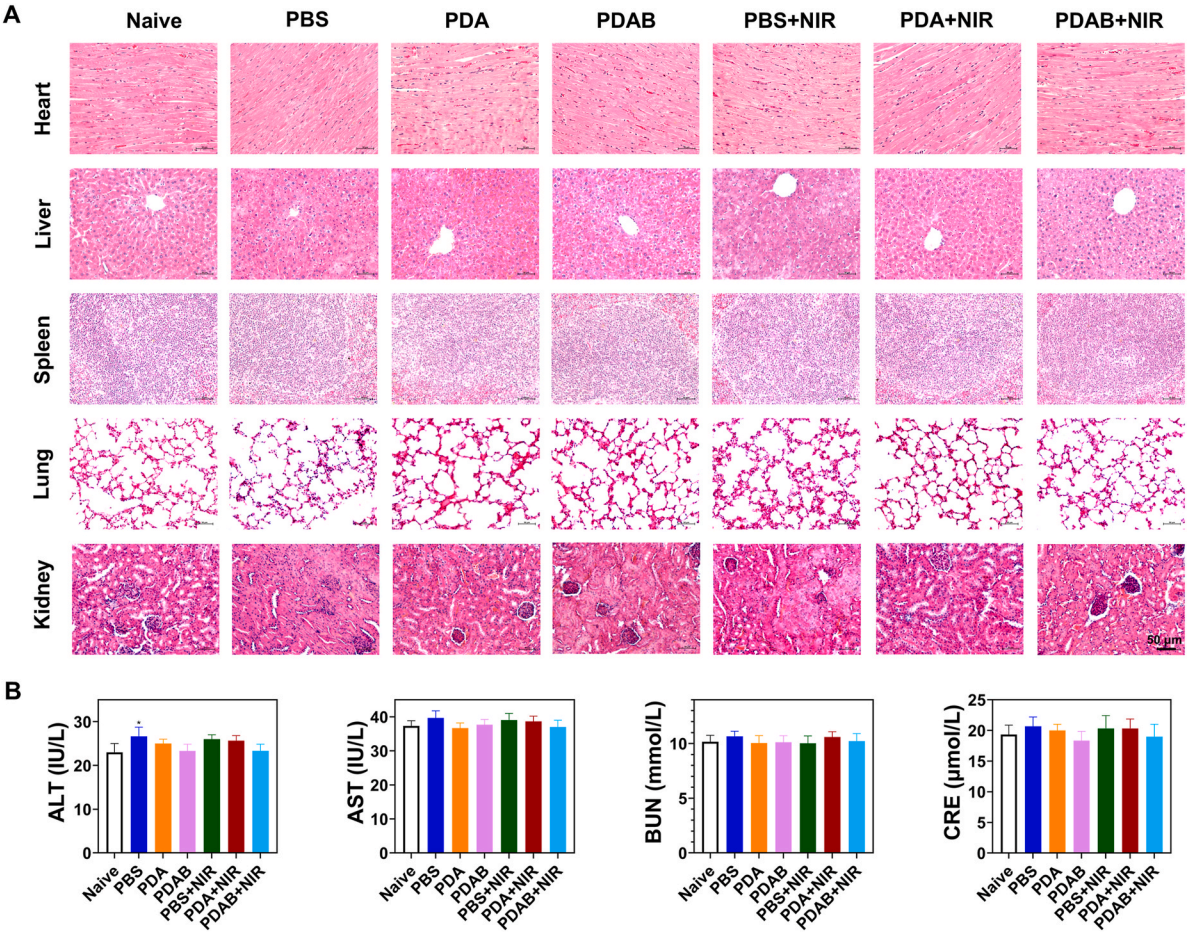

Fig. 7. Biosafety assessment of PDAB. (A) H&E staining sections of the heart, liver, spleen, lungs and kidneys of mice in each group. (B) AST, ALT,BUN and CRE levels in serum of PDAB injected and non-injected mice. Data are expressed as mean ± SD (n = 3). Statistical significance was assessed by a twotailed Student's *t*-test, *p < 0.05.

4. Conclusions

In summary, this study presents a pH- and NIR-responsive hydrogen nanocarrier (PDAB) that enables controlled hydrogen release and efficient ROS scavenging within the RA joint cavity, thereby suppressing RA progression and analgesia. In the AIA model, NIR-activated PDAB nanogenerators enabled sustained intra-articular hydrogen release, effectively scavenging local ROS to suppress inflammation and alleviate clinical symptoms. Concurrently, assessment of pain behaviors and spinal neuronal activation revealed a decoupling between inflammatory mitigation and analgesia, suggesting that hydrogen's analgesic mechanism involves synergistic peripheral anti-inflammation and central sensitization inhibition. Mechanistically, we further demonstrates that hydrogen-induced inhibition of central sensitization was achieved by regulating ROS/NF-κB pathway. This ROS-centric strategy represents a paradigm shift in RA management, overcoming conventional analgesics' limitations against nociplastic pain. Our future work will advance the characterization of spinal dorsal horn neuronal activity through direct electrophysiological assessment. Furthermore, comprehensive delineation of the molecular circuitry governing hydrogen-induced analgesia and systematic characterization of hydrogen's immunomodulatory networks in RA pathogenesis represent imperative research directions.

CRediT authorship contribution statement

Qiong Wu: Writing – original draft, Investigation, Visualization, Formal analysis, Validation, Conceptualization, Writing – review & editing, Methodology. **Jian Zhang:** Methodology, Investigation, Writing – original draft, Formal analysis, Visualization. **Yu Nan:** Methodology, Investigation, Validation. **Shixin Zhang:** Validation, Methodology, Formal analysis. **Yuyang He:** Methodology, Investigation. **Kexin Ye:** Visualization, Methodology. **Xiaowen Ruan:** Methodology, Investigation. **Sai Kishore Ravi:** Methodology, Investigation, Writing – review & editing. **Hushan Wang:** Project administration, Funding acquisition, Conceptualization. **Fangfang Chen:** Writing – review & editing, Project administration, Funding acquisition, Conceptualization.

Declaration of competing interest

The authors declare that they have no known competing financial interests or personal relationships that could have appeared to influence the work reported in this paper.

Acknowledgement

This work was supported by the National Key Research and Development Program of China (2024YFA0918600), the National Natural Science Foundation of China (32271446), Jilin Province Health Science and Technology Capability Improvement Plan Project (2022LC121), the Program for JLU Science and Technology Innovative Research Team (JLUSTIRT, 2019TD-36) and Wu Jieping Medical Foundation (320.6750.17383).

Appendix B. Supplementary data

Supplementary data to this article can be found online at https://doi.org/10.1016/j.mtbio.2025.102068.

Data availability

Data will be made available on request.

References

[1] A.D. Matteo, J.M. Bathon, P. Emery, Rheumatoid arthritis, Lancet 402 (2023) 2019–2033, https://doi.org/10.1016/s0140-6736(23)01525-8.
[2] P.C. Taylor, Pain in the joints and beyond; the challenge of rheumatoid arthritis, Lancet Rheumatol 5 (2023) e351–e360, https://doi.org/10.1016/s2665-9913(23)00094-2.
[3] D.F. McWilliams, O. Dawson, A. Young, P.D.W. Kiely, E. Ferguson, D.A. Walsh, Discrete trajectories of resolving and persistent pain in people with Rheumatoid Arthritis despite undergoing treatment for inflammation: results from three UK cohorts, J. Pain 20 (2019) 716–727, https://doi.org/10.1016/j.jpain.2019.01.001.
[4] Z.R. Locher, B.W. Kirkham, K. Bannister, D.L. Bennett, C.D. Buckley, L.S. Taams, F. Denk, An interdisciplinary perspective on peripheral drivers of pain in rheumatoid arthritis, Nat. Rev. Rheumatol. 20 (2024) 671–682, https://doi.org/10.1038/s41584-024-01155-z.
[5] M.A. Fitzcharles, S.P. Cohen, D.J. Clauw, G. Littlejohn, C. Usui, W. Häuser, Nociplastic pain: towards an understanding of prevalent pain conditions, Lancet 397 (2021) 2098–2110, https://doi.org/10.1016/s0140-6736(21)00392-5.
[6] J. Nijs, S.Z. George, D.J. Clauw, C. Fernández-de-Las-Peñas, E. Kosek, K. Ickmans, J.F. Carnero, A. Polli, E. Kapreli, E. Huysmans, A.I. Cuesta-Vargas, R. Mani, M. Lundberg, L. Leysen, D. Rice, M. Sterling, M. Curatolo, Central sensitisation in chronic pain conditions: latest discoveries and their potential for precision medicine, Lancet Rheumatol 3 (2021) e383–e392, https://doi.org/10.1016/s2665-9913(21)00032-1.
[7] X. Wang, D. Fan, X. Cao, Q. Ye, Q. Wang, M. Zhang, C. Xiao, The role of reactive oxygen species in the Rheumatoid Arthritis-associated synovial microenvironment, Antioxidants 11 (2022) 1153, https://doi.org/10.3390/antiox11061153. Basel.
[8] E.M. Gravallese, G.S. Firestein, Rheumatoid Arthritis - common origins, divergent mechanisms, N. Engl. J. Med. 388 (2023) 529–542, https://doi.org/10.1056/NEJMra2103726.
[9] Y. Yang, L. Guo, Z. Wang, P. Liu, X. Liu, J. Ding, W. Zhou, Targeted silver nanoparticles for rheumatoid arthritis therapy via macrophage apoptosis and Re-polarization, Biomaterials 264 (2021) 120390, https://doi.org/10.1016/j.biomaterials.2020.120390.
[10] M. Cutolo, R. Campitiello, E. Gotelli, S. Soldano, The role of M1/M2 macrophage polarization in Rheumatoid Arthritis synovitis, Front. Immunol. 13 (2022) 867260, https://doi.org/10.3389/fimmu.2022.867260.
[11] W. Jing, C. Liu, C. Su, L. Liu, P. Chen, X. Li, X. Zhang, B. Yuan, H. Wang, X. Du, Role of reactive oxygen species and mitochondrial damage in rheumatoid arthritis and targeted drugs, Front. Immunol. 14 (2023) 1107670, https://doi.org/10.3389/fimmu.2023.1107670.
[12] W. Zhang, Y. Chen, Q. Liu, M. Zhou, K. Wang, Y. Wang, J. Nie, S. Gui, D. Peng, Z. He, Z. Li, Emerging nanotherapeutics alleviating rheumatoid arthritis by readjusting the seeds and soils, J. Contr. Release 345 (2022) 851–879, https://doi.org/10.1016/j.jconrel.2022.04.001.
[13] Y. Huang, G. Wang, L. Ding, Z. Bai, Y. Leng, J. Tian, J. Zhang, Y. Li, Ahmad, Y. Qin, X. Li, X. Qi, Lactate-upregulated NADPH-dependent NOX4 expression via HCAR1/PI3K pathway contributes to ROS-induced osteoarthritis chondrocyte damage, Redox Biol. 67 (2023) 102867, https://doi.org/10.1016/j.redox.2023.102867.
[14] F. Sunzini, A. Schrepf, D.J. Clauw, N. Basu, The biology of pain: through the Rheumatology Lens, Arthritis Rheumatol. 75 (2023) 650–660, https://doi.org/10.1002/art.42429.
[15] I. Lee, H.K. Kim, J.H. Kim, K. Chung, J.M. Chung, The role of reactive oxygen species in capsaicin-induced mechanical hyperalgesia and in the activities of dorsal horn neurons, Pain 133 (2007) 9–17, https://doi.org/10.1016/j.pain.2007.01.035.
[16] Q. Zhang, Y. Ren, Y. Mo, P. Guo, P. Liao, Y. Luo, J. Mu, Z. Chen, Y. Zhang, Y. Li, L. Yang, D. Liao, J. Fu, J. Shen, W. Huang, X. Xu, Y. Guo, L. Mei, Y. Zuo, J. Liu, H. Yang, R. Jiang, Inhibiting Hv1 channel in peripheral sensory neurons attenuates chronic inflammatory pain and opioid side effects, Cell Res. 32 (2022) 461–476, https://doi.org/10.1038/s41422-022-00616-y.
[17] T. Tadokoro, M.B. Hernandez, K. Agashkov, Y. Kobayashi, O. Platoshyn, M. Navarro, S. Marsala, A. Miyanohara, T. Yoshizumi, M. Shigyo, V. Krotov, S. Juhas, J. Juhasova, D. Nguyen, H.K. Skalnikova, J. Motlik, H. Studenovska, V. Proks, R. Reddy, S.P. Driscoll, T.D. Glenn, T. Kemthong, S. Malaivijitnond, Z. Tomori, I. Vanicky, M. Kakinohana, S.L. Pfaff, J. Ciacci, P. Belan, M. Marsala, Precision spinal gene delivery-induced functional switch in nociceptive neurons reverses neuropathic pain, Mol. Ther. 30 (2022) 2722–2745, https://doi.org/10.1016/j.ymthe.2022.04.023.
[18] N. Esteras, O. Kopach, M. Maiolino, V. Lariccia, S. Amoroso, S. Qamar, S. Wray, D. A. Rusakov, M. Jaganjac, A.Y. Abramov, Mitochondrial ROS control neuronal excitability and cell fate in frontotemporal dementia, Alzheimer's Dement. 18 (2022) 318–338, https://doi.org/10.1002/alz.12394.
[19] A. Bittar, J. Jun, J.H. La, J. Wang, J.W. Leem, J.M. Chung, Reactive oxygen species affect spinal cell type-specific synaptic plasticity in a model of neuropathic pain, Pain 158 (2017) 2137–2146, https://doi.org/10.1097/j.pain.0000000000001014.
[20] R. Socodato, C.C. Portugal, T. Canedo, I. Domith, N.A. Oliveira, R.P. Carvalho, J. B. Relvas, M. Cossenza, c-Src deactivation by the polyphenol 3-O-caffeoylquinic acid abrogates reactive oxygen species-mediated glutamate release from microglia and neuronal excitotoxicity, Free Radic. Biol. Med. 79 (2015) 45–55, https://doi.org/10.1016/j.freeradbiomed.2014.11.019.
[21] S. Ashina, C.E. Robertson, A. Srikiatkhachorn, G.D. Stefano, A. Donnet, M. Hodaie, M. Obermann, M.R. Reyes, Y.S. Park, G. Cruccu, L. Bendtsen, Trigeminal neuralgia, Nat. Rev. Dis. Primers 10 (2024) 39, https://doi.org/10.1038/s41572-024-00523-z.
[22] M. Xu, G. Wu, Q. You, X. Chen, The landscape of smart biomaterial-based hydrogen therapy, Adv Sci(Weinh) 11 (2024) e2401310, https://doi.org/10.1002/advs.202401310.
[23] P. Ji, S. Qiu, J. Huang, L. Wang, Y. Wang, P. Wu, M. Huo, J.l. Shi, Hydrolysis of 2D Nanosheets reverses rheumatoid arthritis through anti-inflammation and

osteogenesis, Adv Mater (2024) e2415543, https://doi.org/10.1002/adma.202415543.
[24] C. Xu, S. Wang, H. Wang, K. Liu, S. Zhang, B. Chen, H. Liu, F. Tong, F. Peng, Y. Tu, Y. Li, Magnesium-based micromotors as hydrogen generators for precise Rheumatoid Arthritis therapy, Nano Lett. 21 (2021) 1982–1991, https://doi.org/10.1021/acs.nanolett.0c04438.
[25] Y. You, Y.X. Zhu, J. Jiang, M. Wang, Z. Chen, C. Wu, J. Wang, W. Qiu, D. Xu, H. Lin, J. Shi, Water-enabled H(2) generation from hydrogenated silicon nanosheets for efficient anti-inflammation, J. Am. Chem. Soc. 144 (2022) 14195–14206, https://doi.org/10.1021/jacs.2c04412.
[26] C. Zhang, D.W. Zheng, C.X. Li, M.Z. Zou, W.Y. Yu, M.D. Liu, S.Y. Peng, Z.L. Zhong, X.Z. Zhang, Hydrogen gas improves photothermal therapy of tumor and restrains the relapse of distant dormant tumor, Biomaterials 223 (2019) 119472, https://doi.org/10.1016/j.biomaterials.2019.119472.
[27] W. Chen, H. Liu, F. Song, L. Xin, Q. Zhang, P. Zhang, C. Ding, pH-Switched near-infrared fluorescent strategy for ratiometric detection of ONOO(-) in lysosomes and precise imaging of oxidative stress in Rheumatoid Arthritis, Anal. Chem. 95 (2023) 1301–1308, https://doi.org/10.1021/acs.analchem.2c04175.
[28] Y. Guo, A. Baschieri, F. Mollica, L. Valgimigli, J. Cedrowski, G. Litwinienko, R. Amorati, Hydrogen atom transfer from HOO(.) to ortho-Quinones explains the antioxidant activity of polydopamine, Angew Chem. Int. Ed. Engl. 60 (2021) 15220–15224, https://doi.org/10.1002/anie.202101033.
[29] D.R. Blake, N.D. Hall, P.A. Bacon, P.A. Dieppe, B. Halliwell, J.M. Gutteridge, The importance of iron in rheumatoid disease, Lancet 2 (1981) 1142–1144, https://doi.org/10.1016/s0140-6736(81)90590-0.
[30] H.M. Khojah, S. Ahmed, M.S. Abdel-Rahman, A.B. Hamza, Reactive oxygen and nitrogen species in patients with rheumatoid arthritis as potential biomarkers for disease activity and the role of antioxidants, Free Radic. Biol. Med. 97 (2016) 285–291, https://doi.org/10.1016/j.freeradbiomed.2016.06.020.
[31] Z. Wang, Z. Tong, H. Chen, G. Nie, Jia Hu, W. Liu, E. Wang, B. Yuan, Z. Wang, J. Hu, Photoacoustic/ultrasonic dual-mode imaging for monitoring angiogenesis and synovial erosion in rheumatoid arthritis, Photoacoustics 29 (2023) 100458, https://doi.org/10.1016/j.pacs.2023.100458.
[32] Y. Qin, M.L. Cai, H.Z. Jin, W. Huang, C. Zhu, A. Bozec, J. Huang, Z. Chen, Age-associated B cells contribute to the pathogenesis of rheumatoid arthritis by inducing activation of fibroblast-like synoviocytes via TNF-α-mediated ERK1/2 and JAK-STAT1 pathways, Ann. Rheum. Dis. 81 (2022) 1504–1514, https://doi.org/10.1136/ard-2022-222605.
[33] N.B. Finnerup, R. Kuner, T.S. Jensen, Neuropathic pain: from mechanisms to treatment, Physiol. Rev. 101 (2021) 259–301, https://doi.org/10.1152/physrev.00045.2019.
[34] S. He, V.O. Zambelli, P. Sinharoy, L. Brabenec, Y. Bian, F. Rwere, R.C. Hell, B. S. Neto, B. Hung, X. Yu, M. Zhao, Z. Luo, C. Wu, L. Xu, K.J. Svensson, S. L. McAllister, C.M. Stary, N.M. Wagner, Ye Zhang, E.R. Gross, A human TRPV1 genetic variant within the channel gating domain regulates pain sensitivity in rodents, J. Clin. Investig. 133 (2023) e163735, https://doi.org/10.1172/jci163735.
[35] M. Iftinca, M. Defaye, C. Altier, TRPV1-targeted drugs in development for human pain conditions, Drugs 81 (2021) 7–27, https://doi.org/10.1007/s40265-020-01429-2.
[36] W. Ding, L. Fischer, Q. Chen, Z. Li, L. Yang, Z. You, K. Hu, X. Wu, X. Zhou, W. Chao, P. Hu, T.M. Dagnew, D.M. Dubreuil, S. Wang, S. Xia, C. Bao, S. Zhu, L. Chen, C. Wang, B. Wainger, P. Jin, J. Mao, G. Feng, M.T. Harnett, S. Shen, Highly synchronized cortical circuit dynamics mediate spontaneous pain in mice, J. Clin. Investig. 133 (2023) e166408, https://doi.org/10.1172/jci166408.
[37] L. Marvaldi, N. Panayotis, S. Alber, S.Y. Dagan, N. Okladnikov, I. Koppel, A. D. Pizio, D.A. Song, Y. Tzur, M. Terenzio, I. Rishal, D. Gordon, F. Rother, E. Hartmann, M. Bader, Mike Fainzilber, Importin α3 regulates chronic pain pathways in peripheral sensory neurons, Science 369 (2020) 842–846, https://doi.org/10.1126/science.aaz5875.
[38] R. Poongodi, T.H. Yang, Y. H.n Huang, K.D. Yang, H.Z. Chen, T.Y. Chu, T.Y. Wang, H.C. Lin, J.K. Cheng, Stem cell exosome-loaded Gelfoam improves locomotor dysfunction and neuropathic pain in a rat model of spinal cord injury, Stem Cell Res. Ther. 15 (2024) 143, https://doi.org/10.1186/s13287-024-03758-5.
[39] C.K. Su, C.M. Ho, H.H. Kuo, Y.C. Wen, C.Y. Chai, Sympathetic-correlated c-Fos expression in the neonatal rat spinal cord in vitro, J. Biomed. Sci. 16 (2009) 44, https://doi.org/10.1186/1423-0127-16-44.
[40] B. Halliwell, A. Adhikary, M. Dingfelder, M. Dizdaroglu, Hydroxyl radical is a significant player in oxidative DNA damage in vivo, Chem. Soc. Rev. 50 (2021) 8355–8360, https://doi.org/10.1039/d1cs00044f.
[41] C. Lee, M. Park, W.C. Bhashini, S. Na, C.G. Lee, E. Hwang, G. Yoon, J.K. Lee, D. H. Roh, Y.H. Kwon, J. Yang, S.A. Hughes, J.E. Vince, J.K. Seo, D. Min, T.H. Kwon, Oxidative photocatalysis on membranes triggers non-canonical pyroptosis, Nat. Commun. 15 (2024) 4025, https://doi.org/10.1038/s41467-024-47634-5.
[42] W. He, T. Long, Q. Pan, S. Zhang, Y. Zhang, D. Zhang, G. Qin, L. Chen, J. Zhou, Microglial NLRP3 inflammasome activation mediates IL-1β release and contributes to central sensitization in a recurrent nitroglycerin-induced migraine model, J. Neuroinflammation 16 (2019) 78, https://doi.org/10.1186/s12974-019-1459-7.
[43] Q. Wen, Y. Wang, Q. Pan, R. Tian, D. Zhang, G. Qin, J. Zhou, L. Chen, MicroRNA-155-5p promotes neuroinflammation and central sensitization via inhibiting SIRT1 in a nitroglycerin-induced chronic migraine mouse model, J. Neuroinflammation 18 (2021) 287, https://doi.org/10.1186/s12974-021-02342-5.
[44] A.F. Castañeda, P. Lu, A.C. Geraghty, E. Song, M.H. Lee, J. Wood, M.R. O'Dea, S. Dutton, K. Shamardani, K. Nwangwu, R. Mancusi, B. Yalçın, K.R. Taylor, L. A. Alvarez, K. Malacon, M.B. Keough, L. Ni, P.J. Woo, D.C. Esquivel, A.M. Shaw Toland, J.R. Gehlhausen, J. Klein, T. Takahashi, J. Silva, B. Israelow, C. Lucas, T. Mao, M.A. Peña-Hernández, A. Tabachnikova, R.J. Homer, L. Tabacof, J. T. Mancuso, E. Breyman, A. Kontorovich, D. McCarthy, M. Quezado, H. Vogel, M. M. Hefti, D.P. Perl, S. Liddelow, R. Folkerth, D. Putrino, A. Nath, A. Iwasaki, M. Monje, Mild respiratory COVID can cause multi-lineage neural cell and myelin dysregulation, Cell 185 (2022) 452–2468, https://doi.org/10.1016/j.cell.2022.06.008.